Robotica (2007) volume 25, pp. 409–424. © 2007 Cambridge University Press
doi:10.1017/S0263574706003171 Printed in the United Kingdom

High-speed navigation of unmanned ground vehicles on uneven terrain using potential fields

Shingo Shimoda†,‡, Yoji Kuroda† and Karl Iagnemma†

†*Department of Mechanical Engineering, Massachusetts Institute of Technology, Cambridge, MA 02139, USA*
‡*Biomimetic Control Research Center, RIKEN, Nagoya 463-0003, Japan*

(Received in Final Form: December 7, 2006. First published online: January 18, 2007)

SUMMARY

Many applications require unmanned ground vehicles (UGVs) to travel at high speeds on sloped, natural terrain. In this paper, a potential field-based method is proposed for UGV navigation in such scenarios. In the proposed approach, a potential field is generated in the two-dimensional "trajectory space" of the UGV path curvature and longitudinal velocity. In contrast to traditional potential field methods, dynamic constraints and the effect of changing terrain conditions can be easily expressed in the proposed framework. A maneuver is chosen within a set of performance bounds, based on the local potential field gradient. It is shown that the proposed method is subject to local maxima problems, rather than local minima. A simple randomization technique is proposed to address this problem. Simulation and experimental results show that the proposed method can successfully navigate a small UGV between predefined waypoints at speeds up to 7.0 m/s, while avoiding static hazards. Further, vehicle curvature and velocity are controlled during vehicle motion to avoid rollover and excessive side slip. The method is computationally efficient, and thus suitable for onboard real-time implementation.

KEYWORDS: Mobile robots; Potential fields; Outdoor terrain; Motion planning.

1. Introduction and Related Work

Unmanned ground vehicles (UGVs) are expected to play significant roles in future military, planetary exploration, and materials handling applications.[1,2] Many applications require UGVs to move at high speeds over rough, natural terrain. One important challenge for high-speed navigation lies in avoiding dynamically inadmissible maneuvers (i.e., maneuvers that self-induce vehicle failure due to rollover and excessive side slip).[3] This is challenging as it requires real-time analysis of vehicle dynamics, and consideration of the effects of terrain inclination, roughness, and traction. Another challenge for high-speed navigation lies in rapidly avoiding static hazards such as trees, large rocks or boulders, water traps, etc.[4] Such hazards are often detected at short range (particularly "negative obstacles," or depressions below the nominal ground plane), and thus hazard avoidance maneuvers must be generated very rapidly.

*Corresponding author. E-mail: shimoda@bmc.riken.jp

Artificial potential fields have long been successfully employed for robot control and motion planning due to their effectiveness and computational efficiency. Generally, these methods construct artificial potential functions in a robot's workspace such that the function's global minimum value lies at the robot's goal position and local maxima lie at locations of obstacles. The robot is "pushed" by an artificial force proportional to the potential function gradient at the robot's position, and thus moves toward the goal position while avoiding hazards.

First works based on this approach were performed by Khatib as a real-time obstacle avoidance method for manipulators.[5] Latombe applied potential field methods to the general robot path planning problem, including high d.o.f. manipulators and mobile robots operating at low speeds in structured, planar environments.[6] This work proposed various techniques for implementing potential field-based planning methods that do not suffer from local minima, a classical problem for potential field planners. Ge et al. applied the potential field concept for dynamic control of a mobile robot, with moving obstacles and goal in a structured environment.[7] This work addressed the local minima problem by judiciously choosing appropriate forms of the potential functions. Decision-making logic was also integrated into the motion planning strategy to avoid local minima. Path planning using potential fields has also been applied to parallel computation schemes and nonholonomic systems.[8,9] In summary, potential fields have been applied extensively to the problem of path planning of manipulators and mobile robots operating at low speeds in structured, indoor settings.[10–14] These methods do not consider the effects of terrain inclination, roughness, and traction on UGV mobility, nor do they address the problem of dynamically inadmissible maneuvers.

The application of artificial potential fields to mobile robot navigation in natural terrain has recently been addressed.[15] This approach relies on a vision-based classification algorithm to analyze local terrain and determine the locations of obstacles and nontraversable terrain regions. A conventional potential field planner is then applied to the 2-D traversability map. Since the approach is designed for low-speed operation on relatively flat, lightly cluttered environments it does not consider the effects of terrain inclination, roughness, or traction, nor does it address the problem of dynamically inadmissible maneuvers.

Here, a local reactive navigation method is presented for high-speed UGVs on rough, uneven terrain. In the

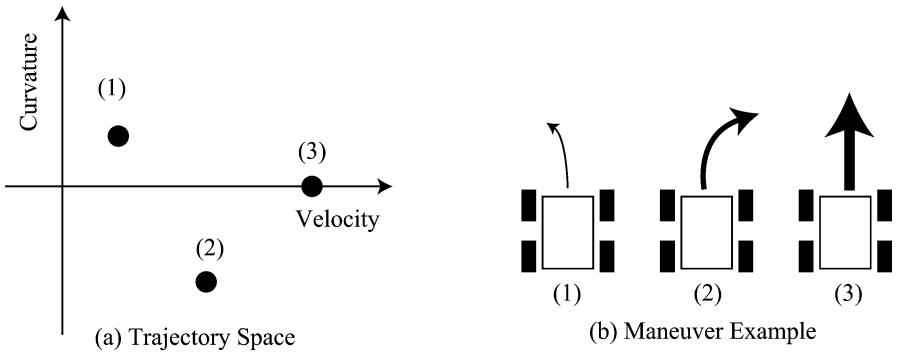

Fig. 1. Trajectory space illustration and maneuver examples corresponding to various locations in the trajectory space.

proposed method, a potential field is defined in the two-dimensional "trajectory space" of the robot's path curvature and longitudinal velocity.[19,20] This is in contrast to other proposed methods, where potential fields are defined in the Cartesian or configuration space. The trajectory space framework allows dynamic constraints, terrain conditions, and navigation conditions (such as waypoint location(s), goal location, hazard location(s), and desired velocity) to be easily expressed as potential functions. A maneuver is chosen within a set of performance bounds, based on the potential field gradient. This yields a desired value for the UGV path curvature and velocity. Desired values for the UGV's steering angle and throttle can then be computed as inputs to low-level tracking controllers.

The proposed approach has some similarity to the dynamic window approach to navigation.[16–18] In that approach, a potential-like field is developed in the 2-dimensional space of translation and rotational velocities, and a behavior is chosen in the space. The method considers goal and obstacle locations, but does not consider dynamic constraints (due to rollover and side slip) and terrain conditions (such as inclination, roughness, and traction).

In Section 2 of this paper, the trajectory space is introduced and problem assumptions are stated. In Section 3, potential functions are defined based on dynamic constraints, terrain conditions, and navigation conditions. In Section 4, the navigation algorithm is outlined. In Section 5, the problems of local minima and maxima are described, and a simple randomization technique for mitigating the effects of these problems is described. In Sections 6 and 7, simulation and experimental results are presented that show that the proposed method can successfully navigate a small UGV between predefined waypoints at speeds up to 7.0 m/s, while avoiding static hazards, vehicle rollover, and excessive side slip. The method is computationally efficient, and thus suitable for onboard real-time implementation.

2. Trajectory Space Description and Problem Assumptions

2.1. Trajectory space description

The trajectory space, $TS \in \Re^2$, is defined as a two-dimensional space of a UGV's instantaneous path curvature and longitudinal velocity.[19,20] This space clearly cannot describe the complete vehicle state, but can rather capture important UGV state and configuration information and serve as a physically intuitive description of the current vehicle status. A UGV's "position" in *TS* is a curvature-velocity pair and is denoted as $\tau = (\kappa, v)$. The relationship of a point in the trajectory space and a vehicle maneuver is shown in Figs. 1(a) and (b). Note that in this work, only positive longitudinal velocities are considered.

The trajectory space is a useful space for UGV navigation for two reasons. First, points in the trajectory space map easily and uniquely to the points in UGV actuation space (generally consisting of one throttle control input and one steering angle control input). Thus, navigation algorithms developed for use in the trajectory space will map to command inputs that obey vehicle nonholonomic constraints. Second, constraints related to dynamic effects such as UGV rollover and side slip are easily expressible in the trajectory space, since these effects are strong functions of the UGV velocity and path curvature.[20] Trajectory space constraints can also be formulated as functions of important terrain parameters, including terrain inclination, roughness, and traction.

In the proposed navigation method, a potential field is constructed in the trajectory space based on dynamic constraints, terrain conditions, and navigation conditions. An appropriate navigation command is then selected based on the properties of this field. Potential field formulation and a navigation methodology are discussed in Section 3.

2.2. Problem assumptions

In this work, it is assumed that the UGV has *a priori* knowledge of the positions of widely spaced (i.e., many vehicle lengths) waypoint and/or goal locations.[3,21,31] Such knowledge is often derived from high-level path planning methods that rely on coarse elevation or topographical map data. It is assumed that the locations of hazards can be locally detected from onboard range sensors, and might take the form of terrain discontinuities such as rocks or ditches, or nongeometric hazards such as soft soil. Hazard detection and sensing issues are important aspects of UGV navigation in natural terrain, but are not a focus of this work.

It is also assumed that estimates of local terrain inclination, roughness, and traction can be sensed or estimated. The inclination of a UGV-sized terrain patch is defined in a body-fixed frame $\boldsymbol{B}$ (see Fig. 2) by two parameters, θ and ϕ, associated with the roll and pitch, respectively, of a plane fit to the patch. Roughness is defined as terrain unevenness

https://doi.org/10.1017/S0263574706003171 Published online by Cambridge University Press

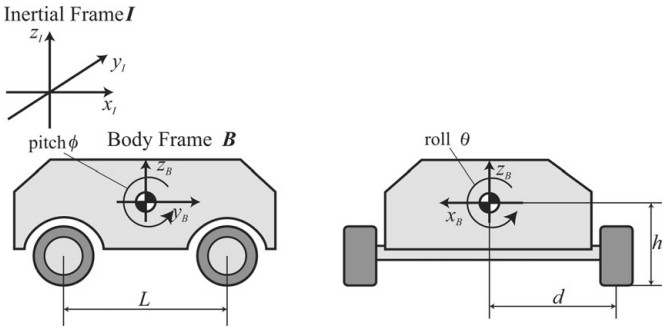

Fig. 2. Definition of a UGV coordinate system.

caused by features that are less than one-half the vehicle wheel radius in size. Roughness is here characterized by the fractal dimension ϖ and is defined over the interval $\varpi \hat{\mathrm{I}} [2, 3]$.[22] The maximum available traction at a wheel-terrain contact point is defined as the product of the terrain friction coefficient μ and the normal force acting on the terrain. This model assumes point contact between the wheel and terrain and neglects nonlinear effects due to wheel slip and terrain and/or tire deformation. Note that estimates of terrain inclination, roughness, and traction can be derived from elevation and visual data via a variety of classification algorithms.[22–26]

The vehicle mass, inertia tensor, center of gravity (c.g.) position, and kinematic properties are assumed to be known with reasonable certainty. The vehicle is assumed to be equipped with inertial and GPS sensors that allow measurement of the vehicle's linear rates and accelerations and position in space with reasonable certainty.

Coordinate systems employed in this work are shown in Fig. 2. A body frame ***B*** is fixed to the vehicle, with its origin at the vehicle center of mass. The position of the vehicle in the inertial frame ***I*** is expressed as the position of the origin of ***B***. The vehicle attitude is expressed by *x*-*y*-*z* Euler angles using the vehicle yaw ψ, roll θ, and pitch ϕ defined in ***B***. (Note that since the UGV suspension is assumed to be rigid, the vehicle roll and pitch are equal to the terrain roll and pitch.) The vehicle wheelbase length is denoted by L, the c.g. height from the ground is h, and the half-width is d. For simplicity, the UGV is here assumed to be axially symmetric.

3. Potential Field Definition

In the proposed method, a potential field is constructed in the trajectory space and vehicle maneuvers are selected based on the properties of this field. The potential field is defined as a sum of potential functions relating to each constraint, hazard, and goal or waypoint location. Here, potential functions are defined for dynamic rollover and side slip constraints, waypoints (and goal) locations, hazard locations, and the desired UGV velocity.

3.1. Potential functions for rollover and side slip constraints

During high-speed operation, a UGV must avoid dynamically inadmissible maneuvers, i.e., maneuvers that self-induce vehicle failure due to rollover and excessive side slip. This is challenging as it requires real-time analysis of vehicle dynamics, and consideration of the effects of terrain inclination, roughness, and traction. Note that although some side slip is expected and unavoidable, substantial slip that causes large heading or path following errors is detrimental. Rollover is also generally undesirable despite the fact that some UGVs are designed to be mechanically invertible.

In the proposed approach, constraint functions related to rollover and side slip are computed from low-order dynamic models and expressed as potential function sources in the trajectory space. Clearly, higher d.o.f. models are available for predicting rollover and side slip, however the proposed models have been shown to be reasonably accurate in practice.[17]

A rollover constraint for a UGV traveling on uneven terrain can be modeled as

$$\kappa_r(v) = \frac{dg_z \pm hg_x}{hv^2} - \delta_r, \tag{1}$$

where κ_r is the maximum admissible path curvature, v is the UGV longitudinal velocity, g^* is the gravitational acceleration of the *-axis direction in ***B***. The two solutions to Eq. (1) correspond to travel on positive/negative inclination side slips, with nonzero g_x components reflecting the effect of terrain roll. Note that δ_r is introduced here as a small positive "safety margin" for reasons described later. A potential function is then defined as

$$PF_r(\kappa, v) = \begin{cases} K_r \left(1 - \dfrac{(\kappa - \kappa_{\max})^2}{(\kappa_r(v) - \kappa_{\max})^2}\right) & \kappa_r < |\kappa| < \kappa_{\max} \\ 0 & 0 \le |\kappa| < \kappa_r \end{cases} \tag{2}$$

where $\kappa_{\max}$ is the maximum attainable path curvature for a UGV based on kinematic steering constraints, and is assumed to be independent of velocity. Here, K_r is a positive gain parameter to modulate the potential function height. The introduction of δ_r in Eq. (1) causes Eq. (2) to be nonzero at curvature-velocity pairs that approach but do not exceed the UGV's predicted stability limit. An illustration of a potential function for the UGV rollover constraint is shown in Fig. 3.

A corresponding repulsive force is generated as the negative gradient of the repulsive potential, as

$$F_r = -\nabla PF_r(k, v) = -\nabla_v PF_r(k, v) - \nabla_\rho PF_r(k, v), \tag{3}$$

where

$$\nabla_v PF_r(\kappa, v) = \begin{cases} 4K_r \dfrac{(\kappa - \kappa_{\max})^2(\kappa_r(v) + \delta_r)}{v(\kappa_r(v) - \kappa_{\max})^3}, & \kappa_r < |\kappa| < \kappa_{\max} \\ 0, & 0 \le |\kappa| < \kappa_r \end{cases}$$

$$\nabla_\rho PF_r(\kappa, v) = \begin{cases} 2K_r \dfrac{(\kappa - \kappa_{\max})}{(\kappa_r(v) - \kappa_{\max})^2}, & \kappa_r < |\kappa| < \kappa_{\max} \\ 0, & 0 \le |\kappa| < \kappa_r. \end{cases} \tag{4}$$

This repulsive force grows increasingly large as the UGV curvature exceeds the maximum allowable curvature defined

https://doi.org/10.1017/S0263574706003171 Published online by Cambridge University Press

in Eq. (1), and is zero otherwise. Thus, the repulsive force affects navigation only when the UGV is on the verge of executing a dynamically inadmissible maneuver due to rollover.

Side slip occurs when the lateral traction forces between a UGV's wheels and the terrain is exceeded by the sum of the centrifugal force and lateral gravitational force component. The maximum path curvature that a UGV can track without excessive side slip can be modeled as follows:

$$\kappa_s(v) = \frac{-g_x \pm \mu g_z}{v^2} - \delta_s, \tag{5}$$

where ρ_s is the maximum admissible path curvature. Again, δ_s is introduced for reasons identical to those described earlier. A potential function is then defined as

$$PF_s(\kappa, v) = \begin{cases} K_s \left(1 - \dfrac{(\kappa - \kappa_{\max})^2}{(\kappa_s(v) - \kappa_{\max})^2}\right), & \kappa_s < |\kappa| < \kappa_{\max} \\ 0, & 0 \le |\kappa| < \kappa_s. \end{cases} \tag{6}$$

Again, K_s is a positive gain parameter to modulate the potential function height. An illustration of a potential function for the side slip constraint appears similar to that for the rollover constraint shown in Fig. 3.

A corresponding repulsive force is generated as the negative gradient of the repulsive potential as

$$F_s = -\nabla PF_s(\kappa, v) = -\nabla_v PF_s(\kappa, v) - \nabla_\rho PF_s(\kappa, v), \tag{7}$$

where

$$\nabla_v PF_s(\kappa, v) = \begin{cases} 4K_s \dfrac{(\kappa - \kappa_{\max})^2(\kappa_s(v) + \delta_r)}{v(\kappa_s(v) - \kappa_{\max})^3}, & \kappa_r < |\kappa| < \kappa_{\max} \\ 0, & 0 \le |\kappa| < \kappa_r \end{cases} \tag{8}$$

$$\nabla_\rho PF_s(\kappa, v) = \begin{cases} 2K_s \dfrac{(\kappa - \kappa_{\max})}{(\kappa_s(v) - \kappa_{\max})^2}, & \kappa_r < |\kappa| < \kappa_{\max} \\ 0, & 0 \le |\kappa| < \kappa_s. \end{cases}$$

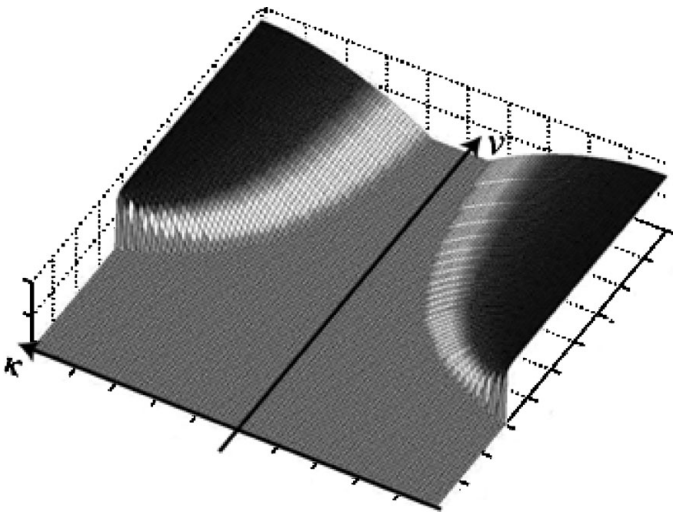

Fig. 3. Illustration of potential function of rollover and side slip constraints.

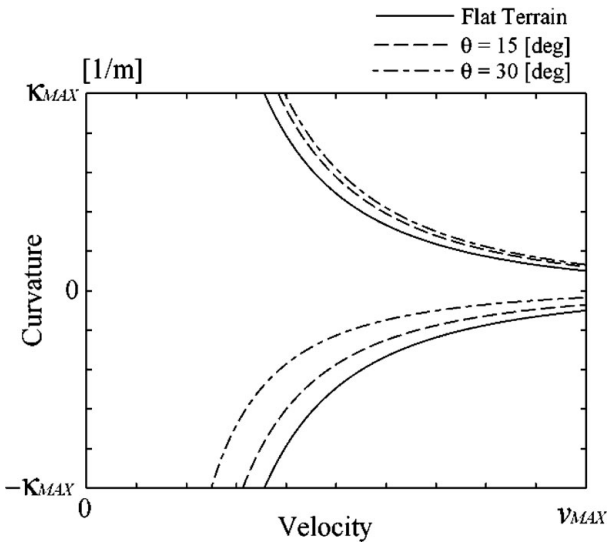

Fig. 4. Illustration of effect of terrain inclination on rollover constraint.

The repulsive force grows increasingly large as the UGV curvature exceeds the maximum allowable curvature defined in Eq. (5), and is zero otherwise. Thus, the repulsive force affects navigation only when the UGV is on the verge of executing a dynamically inadmissible maneuver due to side slip.

The models employed earlier are functions of the terrain inclination and traction. An example of the effects of varying inclination on the constraint equation (1) can be observed in Fig. 4. Here, rollover constraints are shown for the case of flat terrain, rolling terrain with $\theta = 15^\circ$, and rolling terrain with $\theta = 30^\circ$. The solid or dashed lines indicate the point at which the value of Eq. (2) exceeds zero. It can be seen that as terrain inclination increases, the rollover constraint model predicts that a UGV can safely execute negative curvature maneuvers ("downslope" turns) at greater velocity than positive curvature maneuvers ("upslope" turns). This is physically reasonable, since during negative curvature maneuvers the gravity vector g_x component acts counter to centripetal acceleration.

An example of the effect of traction on the constraint equation (5) can be observed in Fig. 5. Here, side slip constraints are shown for the case of flat terrain, with $\mu = 0.2$, 0.6, and 1.0. The solid or dashed lines indicate the point at which the value of Eq. (6) exceeds zero. It can be seen that as terrain traction increases, the side slip constraint model predicts that a UGV can safely execute a fixed-curvature maneuver at greater velocity. Again, this is physically reasonable, since during travel on high-traction terrain the available cornering force is greater than on low-traction terrain. Thus, the proposed potential functions can capture the effects of terrain inclination and traction.

Terrain roughness influences rollover and side slip by inducing variation in the wheel normal forces. It has been shown that for natural terrain, the presence of roughness leads to a distribution of curvature-velocity pairs at which rollover or side slip occurs, with the mean of this distribution approximately described by the prediction from the rigid-body models of Eqs. (1) and (5).[17,28] Monte Carlo simulation

https://doi.org/10.1017/S0263574706003171 Published online by Cambridge University Press

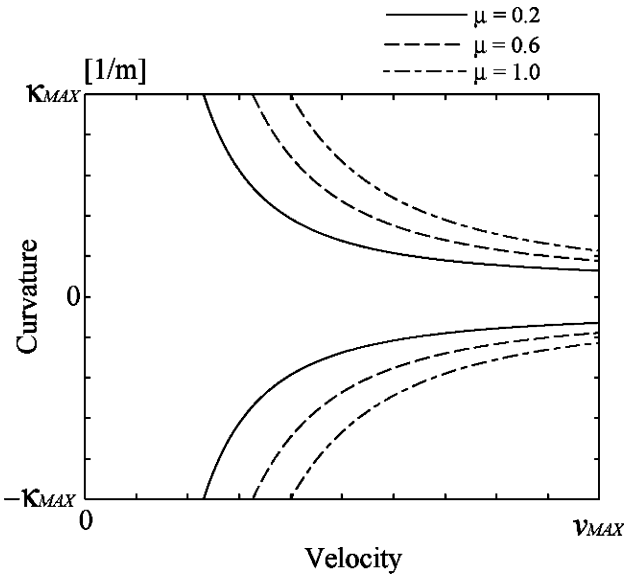

Fig. 5. Illustration of effect of terrain traction on side slip constraint.

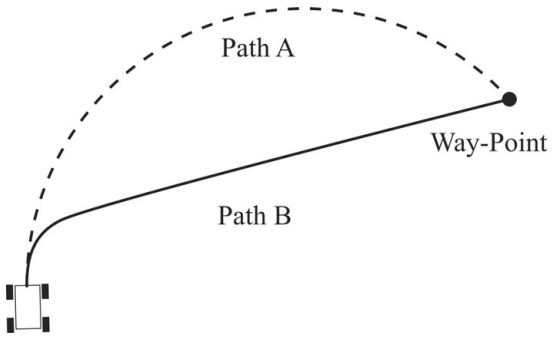

Fig. 6. Comparison of possible UGV paths toward a waypoint.

methods have been developed for analyzing this distribution as a function of terrain roughness.[27,28] Detailed discussion of the effects of terrain roughness on UGV mobility are beyond the scope of this paper.

In practice, probability distribution functions related to rollover and side slip can be determined as a function of terrain roughness via offline Monte Carlo simulation analysis. The parameters δ_r and δ_s can then be chosen to correspond to 3σ limits of these distributions. A look-up table can then be constructed relating δ_r and δ_s to roughness ϖ. Since roughness can be measured online in real time, δ_r and δ_s can be modulated to account for roughness. Thus, the proposed potential functions can be adapted for in rough terrain scenarios if measurements or estimates of terrain roughness are available.

3.2. Potential function for waypoint locations

To enable UGV navigation between waypoints, an attractive potential function is composed with a corresponding attractive force that tends to "pull" the UGV toward the desired waypoint at a given instant. The form of the potential function influences the shape of the resulting UGV path. For example, consider a UGV moving toward a desired waypoint as shown in Fig. 6. Two possible paths to the waypoint are illustrated as paths A and B, resulting from two different potential functions. Both paths possess the same initial curvature. Path B, however, is more direct and thus more desirable than Path A in the absence of other constraints.

To generate direct paths between waypoints, a method illustrated in Fig. 7 is proposed. Let O_d be the Euclidean distance between the UGV c.g. and the waypoint. A line connecting the UGV c.g. and waypoint intersects a circle centered at the UGV c.g. with radius $2\rho_{\max}$. The desired curvature ρ_d to this "virtual waypoint" is taken as the curvature that leads to the intersection point. In the case where $O_d < 2/\kappa_{\max}$, κ_d is taken as the curvature that leads to the waypoint directly.

A potential function corresponding to the current desired waypoint location is then defined as follows:

$$PF_w(\kappa) = K_w(\kappa - \kappa_d)^2, \tag{9}$$

where K_g is a positive gain parameter to modulate the potential function height. An illustration of a potential function for waypoint location is shown in Fig. 8.

A corresponding attractive force is generated as the negative gradient of the attractive potential as

$$F_w = -\nabla_\rho PF_w(\kappa), \tag{10}$$

where

$$\nabla_\rho PF_w(\kappa, v) = 2K_w(\kappa - \kappa_d). \tag{11}$$

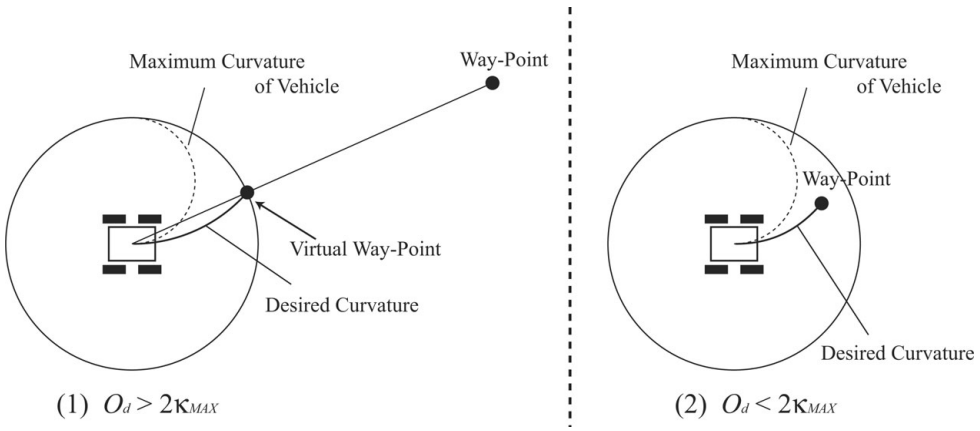

Fig. 7. Computation of desired steering angle using "virtual waypoints."

https://doi.org/10.1017/S0263574706003171 Published online by Cambridge University Press

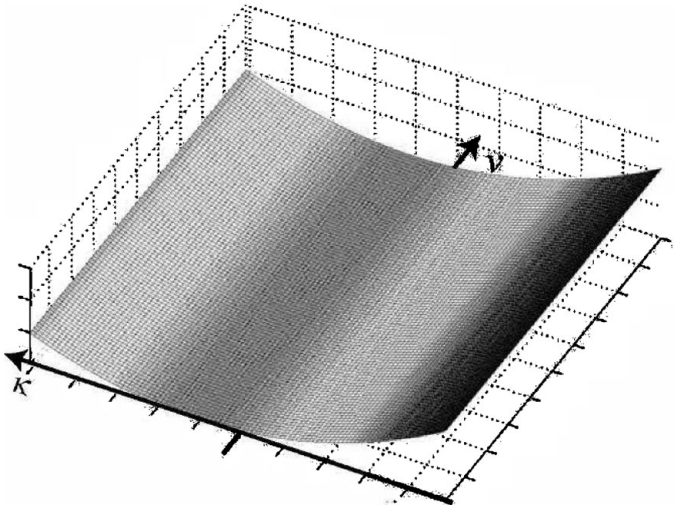

Fig. 8. Illustration of potential function for waypoint location.

The difference in robot trajectories resulting from the use of virtual waypoints is illustrated in a simulation result presented in Section 6.1.

3.3. *Potential function for desired velocity*

A potential function related to the desired UGV velocity can be simply expressed as follows:

$$PF_v(v) = K_v(v - v_d)^3, \tag{12}$$

where v_d is the desired UGV velocity and K_v is a positive gain parameter to modulate the potential function height. Note that v_d may be a function of position or time to reflect high-level objectives. An illustration of the potential function for the desired velocity is shown in Fig. 9.

A corresponding attractive force is generated as the negative gradient of the attractive potential as

$$F_v = -\nabla_v PF_v(v) \tag{13}$$

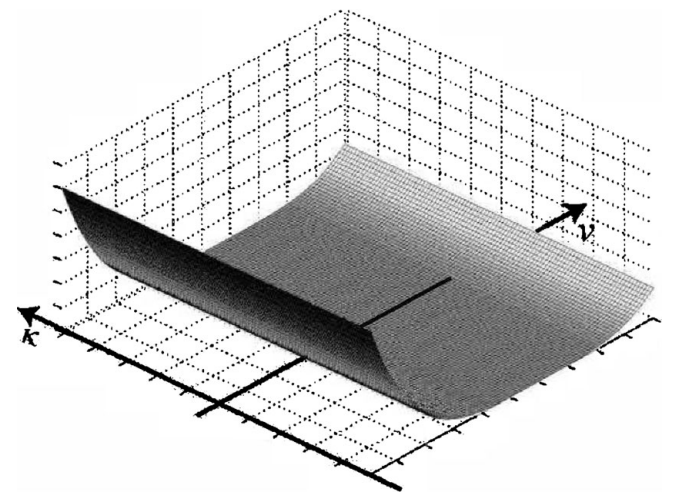

Fig. 9. Illustration of potential function of desired velocity.

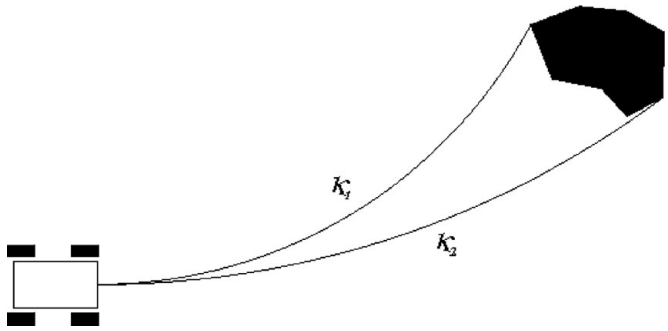

Fig. 10. Minimum and maximum steering angles toward a hazard.

where

$$\nabla_v PF_v(\kappa, v) = 3K_v(v - v_d)^2. \tag{14}$$

3.4. *Potential function for hazard locations*

A potential function related to hazard locations should consider (at minimum) the relative position and orientation of the UGV and hazard(s). Consider the general situation of a UGV approaching a static hazard shown in Fig. 10. Here κ_1 and κ_2 are the maximum and minimum path curvatures toward the hazard from the current UGV position and velocity. A point vehicle representation is assumed and hazard boundaries are computed accordingly.

Here, a potential function for hazard location is proposed that considers several factors. First, path curvatures between κ_1 and κ_2 are undesirable if the UGV is near the hazard, yet can be safely employed if the hazard is distant. Second, the potential function value should be higher at high speed than at low speed since both path tracking accuracy and response time decrease with increasing speed. Third, the orientations of hazard(s) relative to the current waypoint (with respect to the UGV position) should influence the hazard potential function value, thus allowing a UGV to "pass" hazards without being unduly disturbed by them. This is illustrated in Fig. 11.

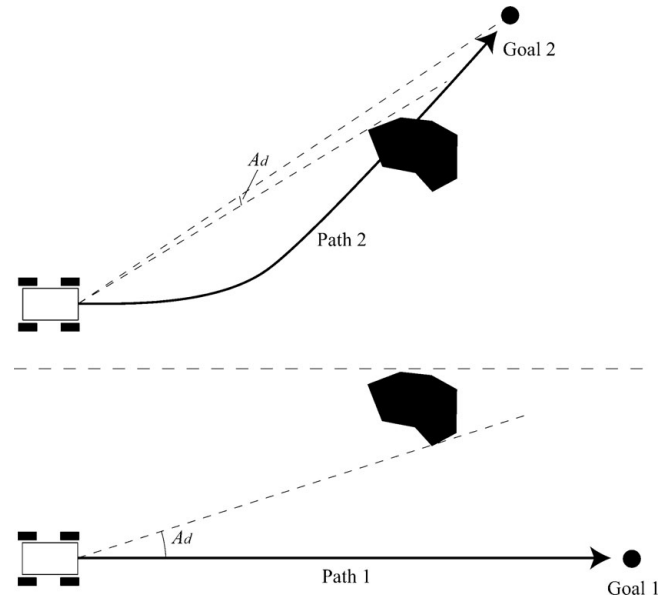

Fig. 11. Influence of relative locations of waypoints and hazards.

https://doi.org/10.1017/S0263574706003171 Published online by Cambridge University Press

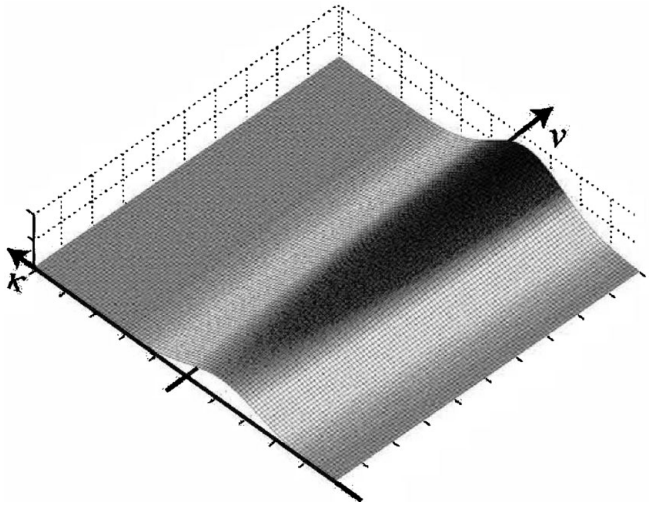

Fig. 12. Illustration of potential function for single hazard location.

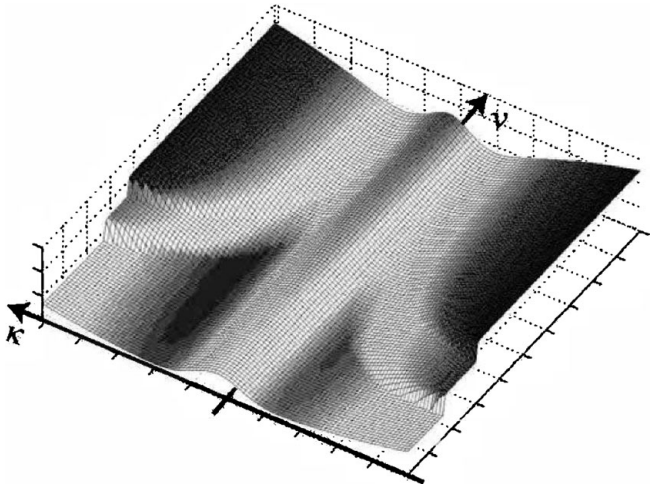

Fig. 13. Illustration of proposed net potential field.

From these observations, a potential function for hazard locations is defined as follows:

$$PF_h(\kappa, v) = \frac{K_h(K_{hv}v+1)}{(K_{hd}O_d+1)(K_{ha}|A_d|+1)} e^{-(\kappa-X)^2/2\sigma^2}, \quad (15)$$

where A_d is the minimum angle between the current waypoint and the hazard of interest (see Fig. 11), $X=(\kappa_1+\kappa_2)/2$, and $\sigma=(\kappa_1-\kappa_2)/2$. K_h, K_{hd}, K_{ha}, and K_{hv} are positive gain parameters to modulate the potential function height.

The hazard potential function is chosen as a scaled Gaussian with σ proportional to the hazard "width" as observed by the UGV at a given distance. As the UGV approaches the hazard or travels at increased speed, the magnitude of the potential function grows. As the heading angle to the hazard relative to the current waypoint diverges, the magnitude of the potential function diminishes. An illustration of the potential function for a UGV approaching a hazard is shown in Fig. 12. Note that a single function is employed for each hazard, and multiple hazards can be described as a summation of multiple functions.

A corresponding repulsive force is generated as the negative gradient of the repulsive potential as

$$F_h = -\nabla PF_h(\kappa, v) = -\nabla_v PF_h(\kappa, v) - \nabla_\rho PF_h(\kappa, v), \quad (16)$$

where

$$\nabla_v PF_h(\kappa, v) = \frac{K_h K_{hv}}{(K_{hd}O_d+1)(K_{ha}|A_d|+1)} e^{-(\kappa-X)^2/2\sigma^2}$$

$$\nabla_\rho PF_h(\kappa, v) = \frac{K_h(K_{hv}v+1)(\kappa-X)}{\sigma(K_{hd}O_d+1)(K_{ha}|A_d|+1)} e^{-(\kappa-X)^2/2\sigma^2}. \quad (17)$$

3.5. Definition of net potential field

A net potential field is generated as the sum of all proposed potential functions as

$$NPF(\kappa, v) = PF_r(\kappa, v) + PF_s(\kappa, v) + PF_w(\kappa) + PF_v(v) + \sum_{i=1}^{n} PF_{hi}(\kappa, v), \quad (18)$$

where n is the number of hazards present and PF_{hi} is the potential function corresponding to the ith hazard. An illustration of a net potential field is shown in Fig. 13.

A net force field corresponding to the net potential field is generated as the sum of all proposed virtual forces

$$NF(\kappa, v) = -\nabla PF_r(\kappa, v) - \nabla PF_s(\kappa, v) - \nabla PF_w(\kappa) - \nabla PF_v(v) - \sum_{i=1}^{n} \nabla PF_{hi}(\kappa, v). \quad (19)$$

4. Navigation Algorithm Description

During navigation, the gradient of the net potential field is computed at the UGV's position in the trajectory space (i.e., its instantaneous path curvature and longitudinal velocity $\tau=(\kappa, v)$). A desired curvature and velocity is then chosen in the direction of maximum descent as $\tau^*=\tau+NF(\tau)$. The desired maneuver τ^* is used to derive command inputs for low-level control of UGV steering angle and throttle. This procedure is repeated at a control rate appropriate to the navigation task, usually 1–10 Hz.

Three factors must be considered during implementation of the proposed algorithm. First, not all regions of *TS* are reachable in a finite time t due to limits on UGV acceleration, deceleration, and steering rate. Thus, τ^* should be chosen in a subspace of *TS* termed the "reachable trajectory space."[20] Second, calculation of the potential functions in Eq. (18) may be corrupted by sensor noise, and thus filtering should be performed during the gradient calculations in Eq. (19). Third, the desired path curvature and velocity must be mapped to steering angle and throttle command inputs to perform low-level control. These factors are discussed later.

4.1. Reachable trajectory space description

The reachable trajectory space is computed based on knowledge of the UGV's instantaneous curvature and velocity, and its acceleration, braking, and steering characteristics. For a UGV located at τ in the trajectory space, an estimate of the maximum and minimum attainable

https://doi.org/10.1017/S0263574706003171 Published online by Cambridge University Press

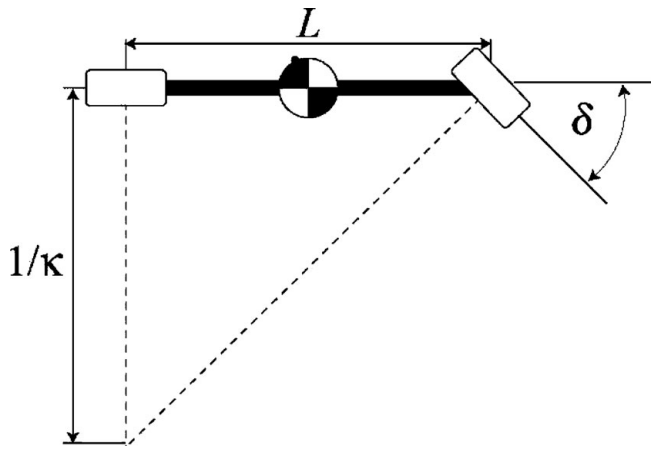

Fig. 14. Single-track UGV model for reachable trajectory space calculation.

velocities in a time t is

$$\begin{aligned} v^{\max}_{\text{reachable}} &= v + a^{+}t \\ v^{\min}_{\text{reachable}} &= v - a^{-}t, \end{aligned} \tag{20}$$

where a^{+} and a^{-} are UGV acceleration/deceleration parameters, respectively, assuming constant acceleration/deceleration capability. The maximum and minimum attainable path curvatures for a front-wheel steered vehicle in time t are

$$\begin{aligned} \kappa^{\max}_{\text{reachable}}(v) &= \kappa + \dot{\kappa}_{\max}t \\ \kappa^{\min}_{\text{reachable}}(v) &= \kappa - \dot{\kappa}_{\max}t, \end{aligned} \tag{21}$$

where $\dot{\kappa}_{\max}$ is the maximum rate of change of path curvature. This parameter can be computed from the single-track vehicle model shown in Fig. 14.[29] In this model, the properties of the front and rear wheel pairs are lumped into single front and rear wheels located on the centerline of the vehicle, and

$$|\dot{\kappa}_{\max}| = \frac{\tan \dot{\delta}_{\max}}{L}, \tag{22}$$

where $\dot{\delta}_{\max}$ is the maximum rate of change of the UGV steering angle. Figure 15 shows an example of the reachable trajectory space.

4.2. Potential field gradient calculation

In practical application of the proposed algorithm, the calculation of the potential functions in Eq. (18) will be corrupted by sensor noise, and thus filtering must be performed during the gradient calculations in Eq. (19). Here a plane-fitting approach is proposed to compute the potential field gradient. This approach was chosen due to its computational efficiency and ability to mitigate the potentially significant effects of noise on the gradient calculation.

In the proposed approach, the reachable trajectory space, which is nominally rectangular, is discretized into nine equal-area rectangular regions. Other discretization geometries and resolutions are possible, however this discretization was found to yield good results in simulation and experimental trials. A maneuver is chosen via the following algorithm:

1. The value of the net potential field at the center of each region is calculated from Eq. (18) (see Fig. 15(a) and (b));
2. A plane fit to the potential field values is calculated and the gradient of the plane is computed (see Fig. 15(c)). The direction of maximum descent is taken as the desired maneuver direction;
3. The desired maneuver τ^{*} is chosen as the point on the boundary of the reachable trajectory space in the direction of the desired maneuver from the current point.

4.3. Command input calculation

To perform low-level control of the UGV, the desired maneuver τ^{*} is mapped to a pair of command inputs for the UGV steering angle and throttle setpoint. Assuming a single-track vehicle model (see Fig. 14), the steering angle can be computed from the path curvature as

$$\delta = \tan^{-1}(L\kappa). \tag{23}$$

The desired maneuver velocity can be used directly as a low-level control setpoint, assuming a velocity controlled vehicle. A variety of low-level control laws can then be employed to track the desired curvature and velocity. In this work, simple PD compensators were employed.

5. Local Minimum Problem Discussion

5.1. Conventional local minimum description

The existence of local minima is a fundamental problem associated with potential fields constructed from multiple

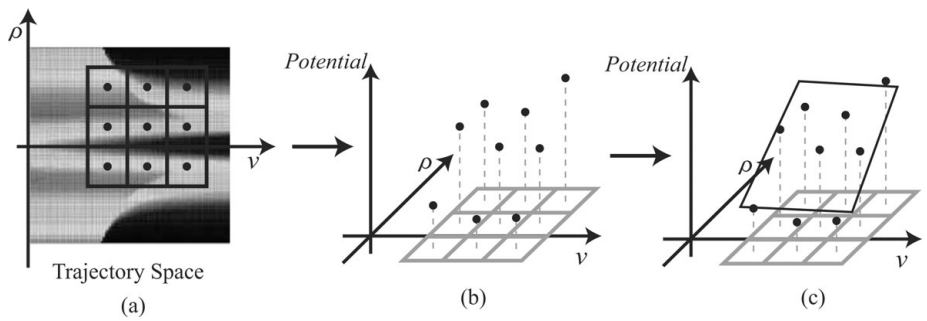

Fig. 15. Illustration of gradient calculation algorithm.

https://doi.org/10.1017/S0263574706003171 Published online by Cambridge University Press

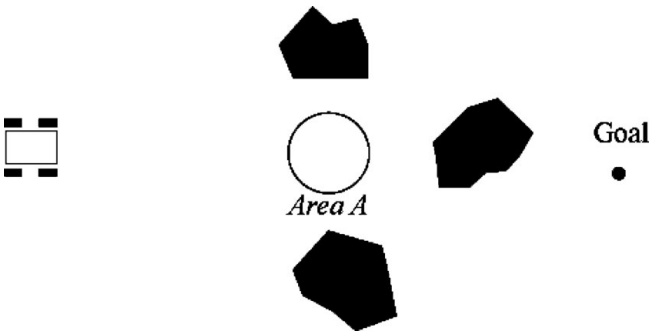

Fig. 16. Example of conventional local minimum.

Fig. 17. Example of conventional free-path local minimum.

potential functions. A classical local minimum situation for Cartesian space potential field methods is illustrated in Fig. 16. Due to the interaction of the repulsive and attractive potential functions associated with the hazard and goal, Area A is a possible location of a local minimum. In Cartesian space potential field applications, this would result in the robot stopping in Area A and not the goal location.

A second situation is shown in Fig. 17. Here, the goal is located between the UGV and a hazard, and the waypoint lies within the region of influence of the hazard potential function. In this case, the global minimum of the potential field is not the waypoint position. A UGV might reach this global minimum yet not reach the waypoint. This situation is called a "free-path local minimum."

5.2. Trajectory space local maximum and minimum description

Situations that lead to local minimum situations in classical potential field approaches often lead to local maximum situations in the proposed method. For example, Fig. 18 shows a situation similar to that shown in Fig. 16, with

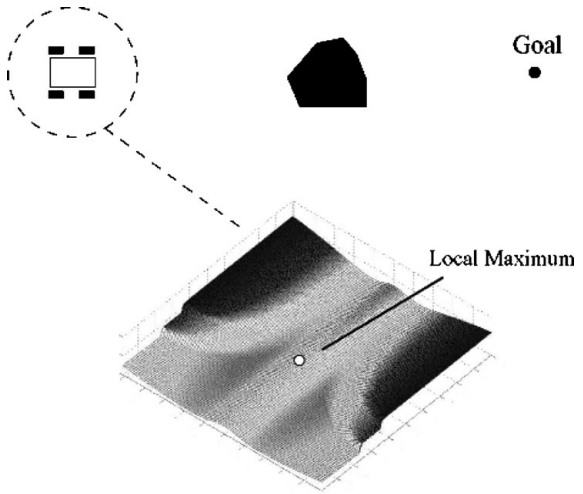

Fig. 18. Example of trajectory space local maximum.

a corresponding trajectory space potential field. In this situation, $\tau = (0,\ v_d)$, $\kappa_d = 0$, $X = 0$, $A_d = 0$, $\theta = \phi = 0^\circ$, and $\mu = 1.0$. Thus, only the hazard potential function influences computation of τ^*. In this situation, the hazard potential function of Eq. (15) becomes

$$PF_h(\kappa,\ v) = \frac{K_h(K_{hv}v + 1)}{K_{hd}O_d + 1} e^{-\kappa^2/2\sigma^2} \tag{24}$$

and $\nabla_\rho PF_h(0,\ v_d) = 0$. Thus, the symmetry of the hazard potential function causes the potential field gradient to be zero in the curvature dimension, and the desired maneuver directs the UGV toward the hazard.

Local maxima are unlikely to occur in practice since sensor noise, terrain unevenness, and terrain inclination all tend to introduce asymmetry to the net potential field. However, to address this issue, Gaussian random noise of small amplitude is added to each element of the net potential field during the algorithm described in Section 4.2. This method serves to perturb unstable local maxima, and avoid situations such as that shown in Fig. 18. It has been observed empirically that the addition of a small amount of random noise does not degrade navigation performance.

An example of the effect of this method is shown in Fig. 19. Here, a situation similar to that shown in Fig. 16 is presented. In this case, however, the addition of noise causes the UGV to be perturbed from the (unstable) local maxima in the trajectory space, and select a maneuver that leads to successful navigation to the goal.

The existence of local minima is possible when a UGV encounters multiple hazards. In contrast to Cartesian space methods, a trajectory space local minima does not result in the UGV stopping at a location that is not the goal location (save for cases where $v = 0$). Rather, the UGV continues to move at the curvature and velocity corresponding to the local minima point. Thus, the trajectory space net potential function is continually changing, even if the UGV is "trapped" in a local minima.

As has been noted by previous researchers, a simple method for addressing these situations is to continue moving according to the total virtual force until the relative positions of the hazards have eliminated the existence of the local minimum.[7] Since the potential function is continually changing, it is highly likely that the local minima will migrate or vanish over time. Though simple, this "waiting" method has been found to be effective in practice.

Another potential type of local minimum that can occur is a limit cycle, where the vehicle follows the same trajectory permanently, usually due to the presence of dense obstacles. Methods for avoiding such limit cycles have been developed by previous researchers.[32]

6. Simulation Results

Simulations were conducted of a small four-wheeled UGV traveling at high speeds over uneven terrain using Matlab and the dynamic simulation software ADAMS 12.0. ADAMS is a multibody simulation engine that allows simulation of high d.o.f. systems on uneven terrain. The UGV was modeled as a front-wheel steered vehicle with a mass of 3.1 kg and independent spring-damper suspensions with

https://doi.org/10.1017/S0263574706003171 Published online by Cambridge University Press

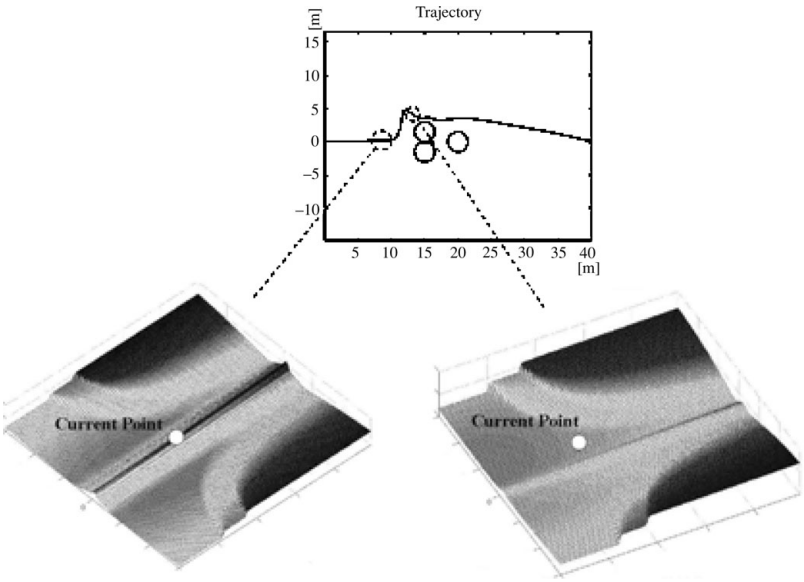

Fig. 19. Example of local maximum avoidance by addition of noise.

linear stiffness and damping parameters $k = 500.0$ N/m and $b = 110$ N s/m, respectively. The UGV length $L = 0.27$ m, the half-width $d = 0.124$ m, the height of UGV c.g. from ground $h = 0.055$ m, and the wheel diameter was 0.12 m.

Wheel–terrain contact forces were derived from the magic tire model using standard parameters for a passenger vehicle tire operating on asphalt.[30] This model is generally accepted for modeling onroad mobility, and was assumed to be a reasonable model for offroad mobility when soil deformation is small. Terrain roughness was created using fractal techniques, with fractal number of 2.05, grid spacing of 2 wheel diameters, and height scaling of 35 wheel diameters.[18] This corresponds to flat but bumpy terrain. Potential function gain parameters were chosen empirically to balance the relative contributions of the various potential functions to the net potential field. The parameter values were set as follows: $K_r = 800$, $K_s = 800$, $K_w = 0.3$, $K_v = 0.5 \times 10^{-5}$, $K_h = 1500$, $K_{hd} = 0.05$, $K_{ha} = 10$, $K_{hv} = 0.07$. These parameters were derived from analysis of simulation studies. Good performance of the algorithm was observed to exist across a range of parameters.

6.1. *Effect of virtual waypoints*

Figure 20 shows a simulation result illustrating the effect of using virtual waypoints (see Section 3.2). Here, the UGV began at $(x, y) = (0.0, 0.0)$ and a single waypoint was set at $(x, y) = (15.0, 15.0)$. Paths resulting from the use of virtual waypoints are in general more direct than paths resulting from widely spaced user-defined waypoints. In this result, the total length of the trajectory employing virtual waypoints was 21.4 m compared to 22.8 m without using virtual waypoints.

6.2. *Obstacle avoidance and waypoint navigation*

Numerous simulations were performed to study the algorithm's ability to guide a UGV at high speed among multiple waypoints while avoiding multiple hazards on flat terrain. Results from a representative simulation are shown

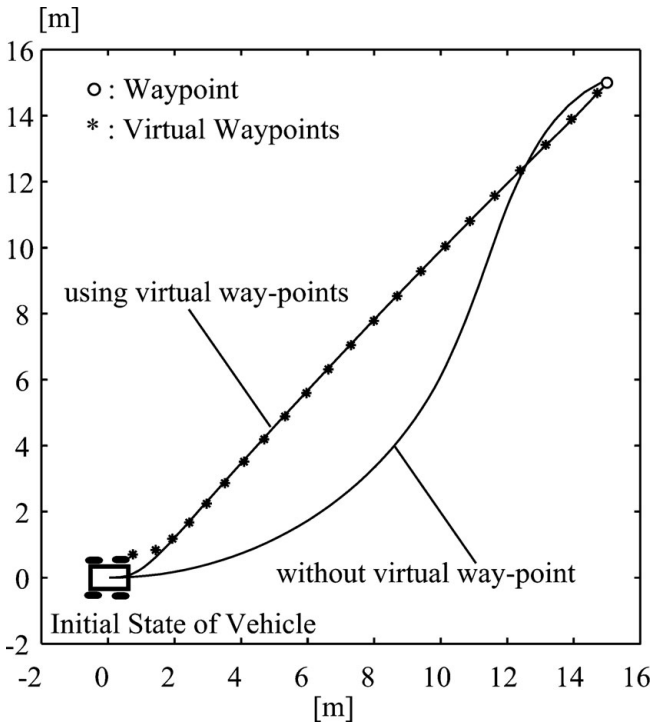

Fig. 20. Influence of virtual waypoint.

in Figs. 21–23. Here, the UGV began at $(x, y) = (0.0, 0.0)$, hazards were set at $(x, y) = \{(15.0, 0.0), (50.0, 22.0)\}$, and waypoints were set at $(x, y) = \{(30.0, 0.0), (40.0, 20.0), (60.0, 20.0)\}$. PD control was employed for steering angle and velocity control. The desired velocity during this simulation was 5.0 m/s. For this small vehicle at this speed, both rollover and significant side slip were possible.

Figure 21 shows the UGV Cartesian space trajectory and shape of the potential field at two locations. The vehicle safely navigated between three waypoints while avoiding two hazards. Figure 22 shows that the velocity remained near the desired value of 5.0 m/s except during turns of large curvature

https://doi.org/10.1017/S0263574706003171 Published online by Cambridge University Press

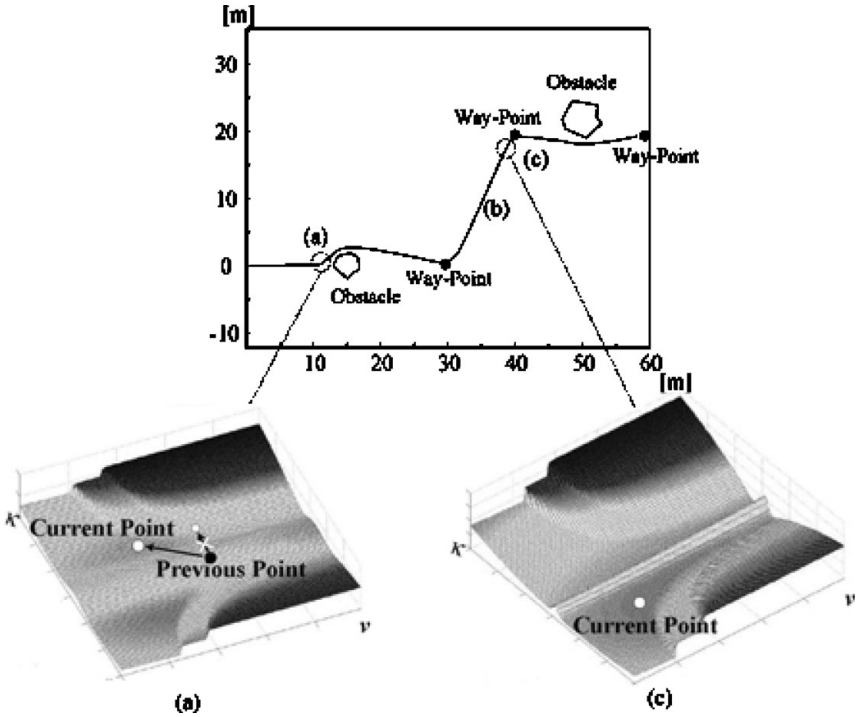

Fig. 21. Map and sample trajectory spaces of simulation result.

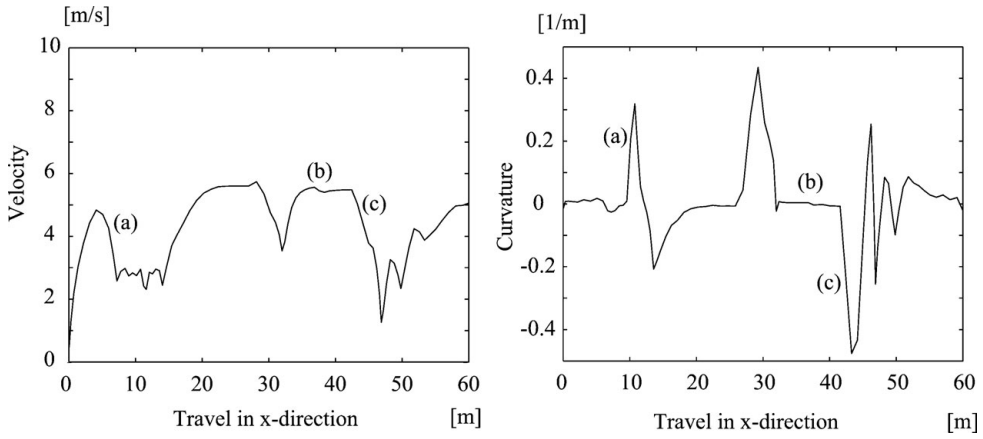

Fig. 22. UGV velocity and curvature—simulation results.

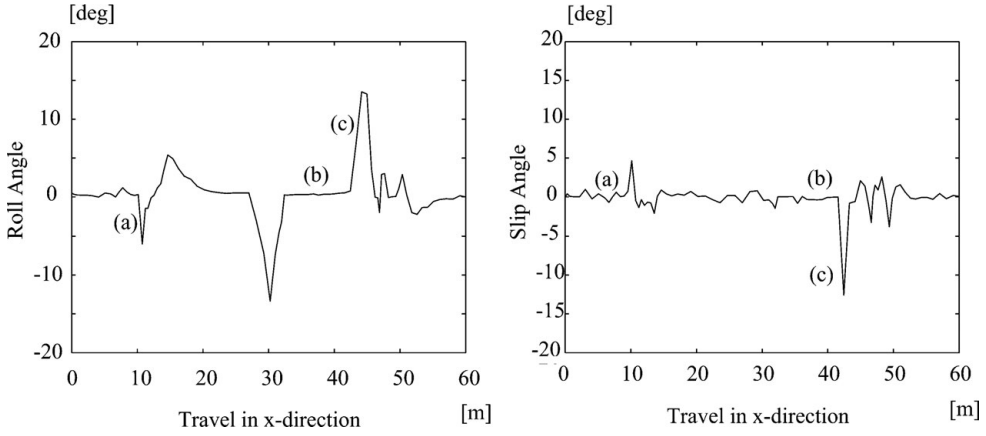

Fig. 23. UGV roll angle and slip angle—simulation results.

https://doi.org/10.1017/S0263574706003171 Published online by Cambridge University Press

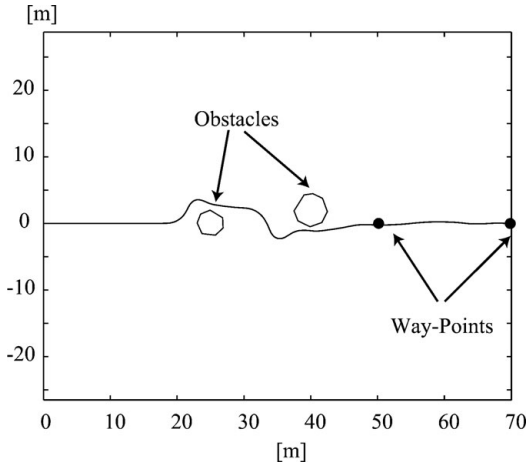

Fig. 24. Map and trajectory of simulation result for desired velocity of 5.0 m/s.

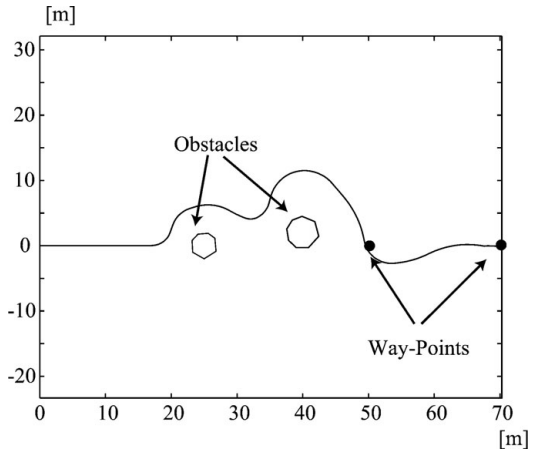

Fig. 26. Map and trajectory of simulation result for desired velocity of 7.0 m/s.

(points (a), (b), and (c)). During these turns, the rollover and/or side slip potential functions caused the velocity to decrease in order to avoid a dynamically inadmissible maneuver. Figure 23 shows plots of the UGV roll angle and slip angle during the trajectory. Slip angle refers to the difference of the angle between the UGV velocity vector at the c.g. and the longitudinal axis of the vehicle. Due to the UGV's relatively high speed, the maximum values of roll angle and slip angle are large, but did not lead to a dynamically inadmissible maneuver.

6.3. Effect of velocity on navigation

Simulations were performed to study the effect of desired UGV velocity on algorithm performance. A map of a representative simulation is shown in Fig. 24. Hazards are located at $(x, y) = \{(25.0, 0.0), (40.0, 2.0)\}$ and waypoints are set at $(x, y) = \{(50.0, 0.0), (70.0, 0.0)\}$. Vehicle and terrain parameters were identical to those in the simulation in Section 6.1.

Simulation results are shown in Figs. 25 and 26 for the case where the desired UGV velocity was 5.0 m/s. As in the simulations of Section 6.1, the UGV velocity decreased at regions of large path curvature in order to avoid dynamically inadmissible maneuvers. The UGV safely navigated between two waypoints while avoiding two hazards.

In contrast, Figs. 27 and 28 show results from a simulation of a UGV traveling through identical terrain with the same hazard and waypoint locations, now with a desired velocity of 7 m/s. In this case, the UGV successfully skirted both of the hazards and reached both waypoints. The overall path differed significantly from the previous simulation, however, due to the increased speed of the UGV and the correspondingly reduced achievable path curvature. However, the UGV safely navigated at a relatively high speed while avoiding rollover or significant side slip.

6.4. Effect of terrain inclination on algorithm performance

Simulations were performed to study the effect of terrain inclination on algorithm performance. An illustration of the scenario is shown in Fig. 28. The hazard and waypoint locations are identical to those in the scenario presented in Section 6.2, however, here the terrain was inclined at a roll angle of 20°. With respect to the UGV's initial orientation. Vehicle and terrain parameters were identical to those in the previous simulations. The desired UGV velocity was 5.0 m/s.

Simulation results are shown in Figs. 29 and 30. The resulting UGV trajectory shown in Fig. 29 differs significantly from the flat-terrain case (see Fig. 24) due to the effect of terrain inclination on trajectory space rollover and side slip constraints. As expected, the UGV executed a

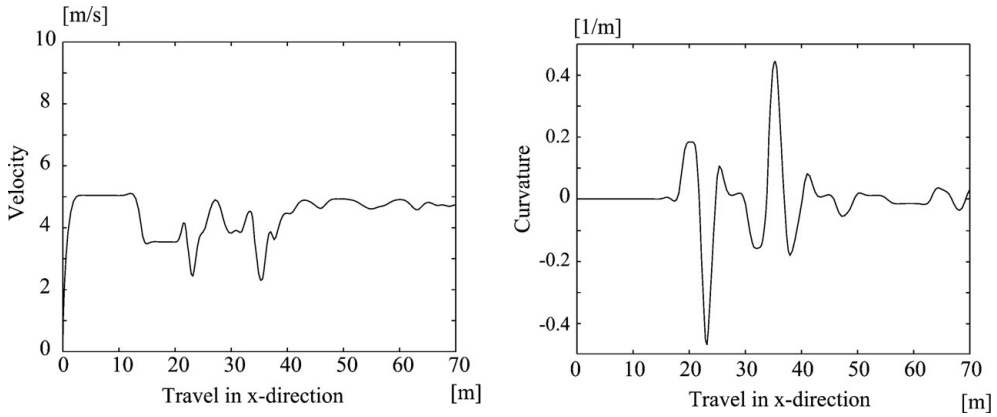

Fig. 25. UGV velocity and curvature for desired velocity of 5.0 m/s.

https://doi.org/10.1017/S0263574706003171 Published online by Cambridge University Press

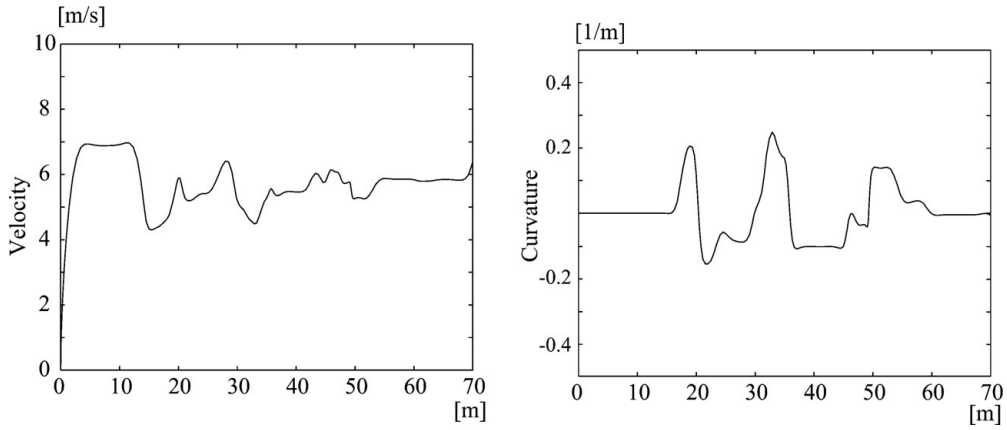

Fig. 27. UGV velocity and curvature for desired velocity of 7.0 m/s.

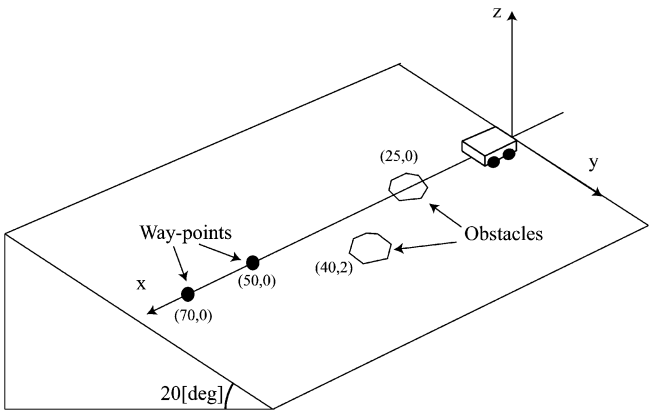

Fig. 28. Illustration of scenario for terrain inclination analysis.

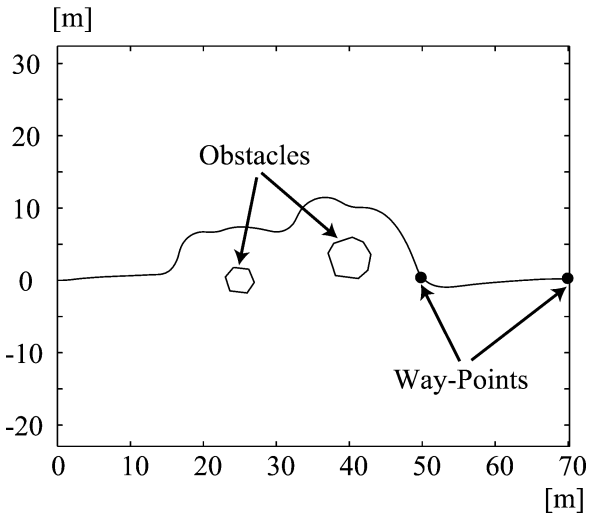

Fig. 29. Trajectory of simulation result for terrain inclination of 20.

safe "downslope" maneuver due to potential field asymmetry caused by terrain inclination. As in the simulations of Section 6.1, UGV velocity decreased at regions of large path curvature to avoid dynamically inadmissible maneuvers (see Fig. 30). This result highlights the algorithm's ability to safely navigate a UGV even on steeply inclined terrain.

7. Experimental Results

A limited number of proof-of-concept experiments were performed to study the algorithm's effectiveness in rough, natural terrain. Experiments were performed on the UGV ARTEMIS, shown in Fig. 31.[20] ARTEMIS is a four-wheeled front-wheel steered vehicle equipped with a Zenoah G2D70 gasoline engine, 700 MHz Pentium III PC-104 onboard computer, Crossbow AHRS-400 INS, a tachometer to measure wheel angular velocity, 20 cm resolution DGPS, and Futaba steering and throttle control servos. The UGV length $L = 0.56$ m, the half-width $d = 0.29$ m, the height of UGV c.g. from ground $h = 0.26$ m, and the wheel diameter was 0.25 m. The body mass was 28.0 kg and the mass of each wheel was 1.85 kg. Experiments were conducted on flat, bumpy terrain covered with grass with an estimated $\mu = 0.8$. In each experiment, the UGV initial position was the origin of the inertial frame, with initial heading aligned with the x axis. Unfortunately, due to hardware malfunctions, only a limited number of experiments were performed.

First, experiments were conducted to study high-speed hazard avoidance. A hazard with 1.0 m radius was set at $(x, y) = (15.0, 0.0)$ and a waypoint was set at $(x, y) = (30.0, 0.0)$. The desired velocity was set at 4.0 m/s. For the ARTEMIS UGV, rollover can occur at speeds above 3.5 m/s.

Results from the experiment are shown in Figs. 32–34. The UGV trajectory is shown in Fig. 32. It can be seen that the UGV successfully avoided the hazard and reached the waypoint. UGV velocity and curvature profiles are shown in Fig. 33. The UGV roll angle profile is shown in Fig. 34. As in the simulation studies, the velocity decreased at periods of large curvature (i.e., around $x = 15.0$ m) and was controlled to near 4.0 m/s in hazard-free regions (i.e., after $x = 25.0$ m). Finally, the vehicle navigated without rollover or side slip. Each computation cycle, involving construction of the net potential field and selection of a maneuver, required approximately 50 ms.

Other experiments were conducted to study high-speed navigation between multiple waypoints. Three waypoints were set at $(x, y) = \{(25.0, 0.0), (30.0, 10.0), (40.0, 10.0)\}$. The desired velocity was 4.0 m/s. The target waypoint was indexed when the UGV moved to within 2.0 m of the current waypoint. An experimental result is shown in Figs. 35–37.

https://doi.org/10.1017/S0263574706003171 Published online by Cambridge University Press

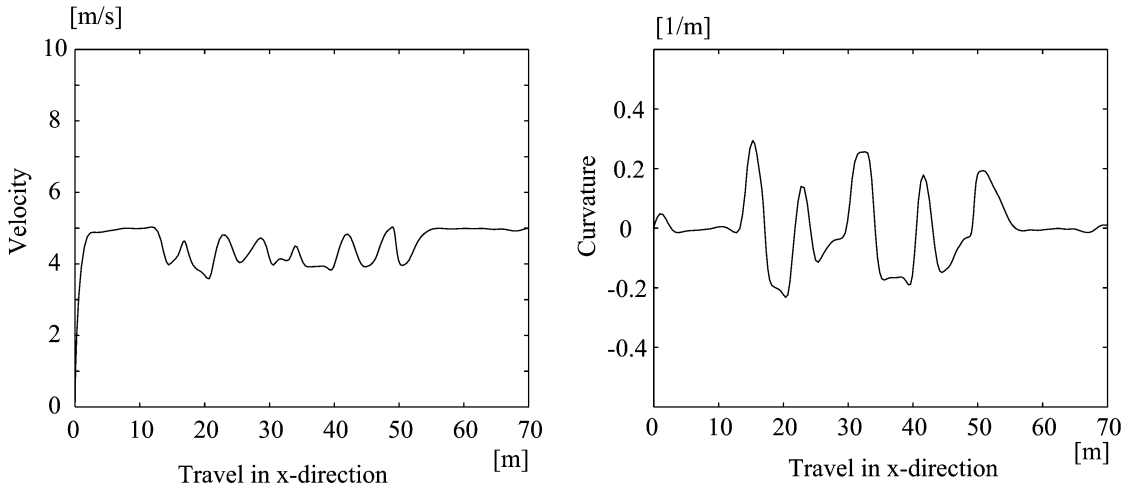

Fig. 30. UGV velocity and curvature for terrain inclination of 20.

Fig. 31. ARTEMIS experimental UGV on outdoor terrain.

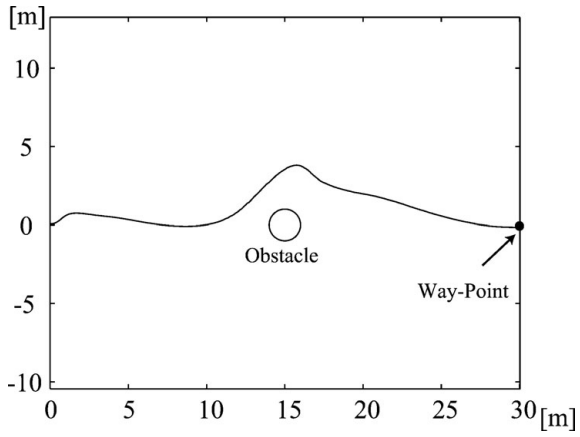

Fig. 32. GPS trajectory of hazard avoidance experiment.

Figure 35 shows that the vehicle successfully navigated between waypoints and reached the goal location. Figure 36 shows that the velocity was controlled near 4.0 m/s, and decreased during periods of large curvature. The UGV roll angle profile is shown in Fig. 37. Again, the vehicle navigated without rollover or side slip. These results suggest that the proposed method can be used for real-time navigation of a UGV at high speeds.

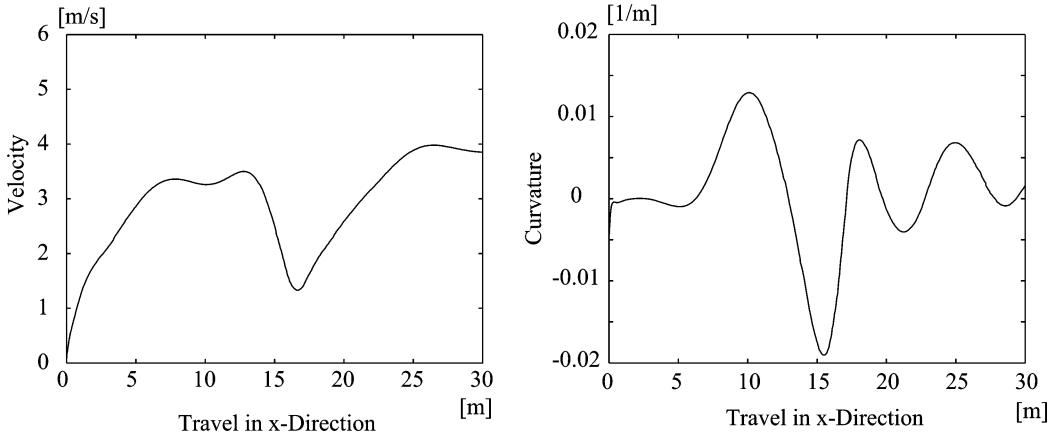

Fig. 33. Velocity and curvature of hazard avoidance experiment.

https://doi.org/10.1017/S0263574706003171 Published online by Cambridge University Press

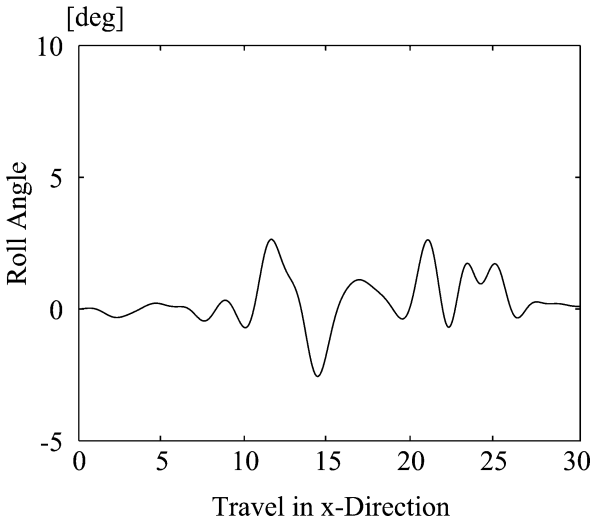

Fig. 34. UGV roll angle of hazard avoidance experiment.

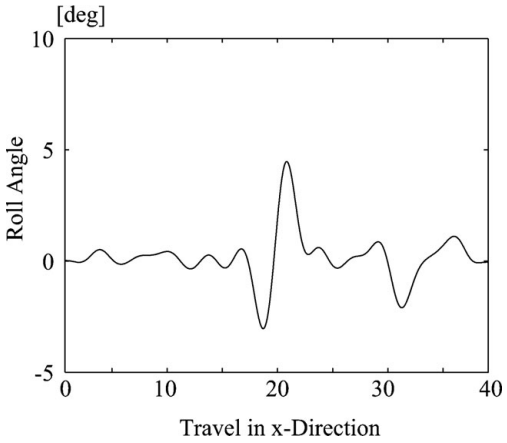

Fig. 37. UGV roll angle of waypoint navigation experiment.

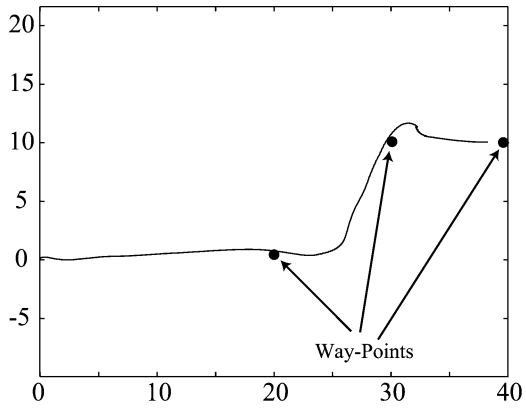

Fig. 35. Trajectory of waypoint navigation experiment.

space defined by a UGV instantaneous path curvature and longitudinal velocity. Dynamic constraints, terrain conditions, and navigation conditions can be expressed in the proposed potential field framework. A maneuver is chosen within a set of performance bounds, based on the local potential field gradient. Issues related to local minima and maxima were discussed, and it was shown that a simple randomization technique can be employed to address these problems. Simulation and experimental results demonstrated the effectiveness of the method in rough, natural terrain. The method is computationally efficient, and thus suitable for onboard real-time implementation. Current research involves experimental validation of the method on highly rough outdoor terrain.

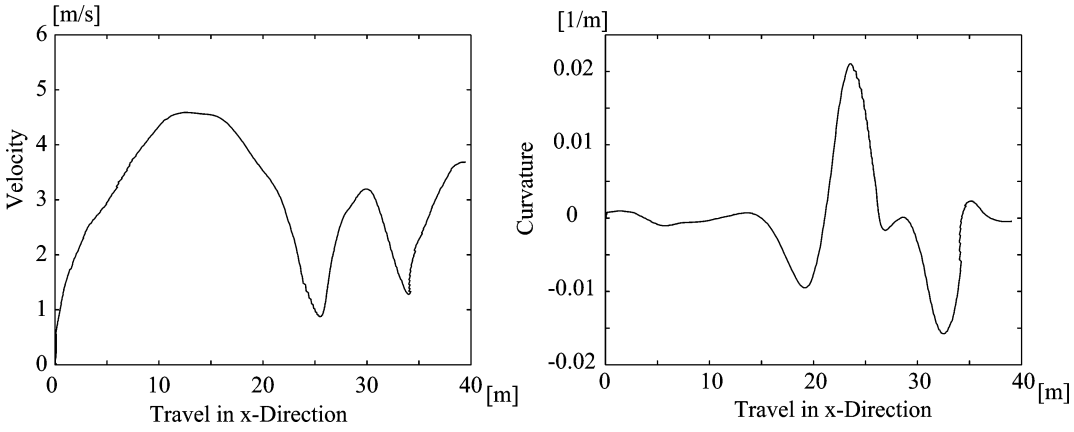

Fig. 36. Velocity and curvature of waypoint navigation experiment.

8. Conclusions

This paper has presented a novel potential field-based method for high-speed navigation of UGVs on rough terrain. The potential field is constructed in the trajectory

Acknowledgments

The authors would like to thank Matthew Spenko for his assistance in performing the experiments presented in this paper. This research was supported by the U.S. Army

https://doi.org/10.1017/S0263574706003171 Published online by Cambridge University Press

Tank-Automotive and Armaments Command and the Defense Advanced Research Projects Agency.

References

1. J. Walker, "Unmanned ground combat vehicle contractors selected," *DARPA News Release* (February 7, 2001), available at www.darpa.mil
2. G. Gerhart, R. Goetz and D. Gorsich, "Intelligent Mobility for Robotic Vehicles in the Army after Next," *Proceedings of the SPIE Conference on Unmanned Ground Vehicle Technology* (1999) pp. 128–139. Orland, FL, USA.
3. Z. Shiller and J. Chen, "Optimal Motion Planning of Autonomous Vehicles in 3-Dimensional Terrains," *Proceedings of the IEEE International Conference on Robotics and Automation* (1990) pp. 198–203.
4. A. Kelly and A. Stents, "Rough terrain autonomous mobility — Part 1: A theoretical analysis of requirements," *Auton. Robots* **5**, 129–161 (1998).
5. O. Khatib, "Real-time obstacle avoidance for manipulators and mobile robots," *Int. J. Robot. Res.* **5**(1), 90–98 (1986).
6. J. Barraquand, B. Langlois and J. Latombe, "Numerical potential field techniques for robot path planning," *IEEE Trans. Syst. Man Cybern.* **22**(2), 224–241 (1992).
7. S. Ge and Y. Cui, "Dynamic motion planning for mobile robots using potential field method," *Auton. Robots* **13** (2002).
8. S. Caselli, M. Reggiani, and R. Sbravati, "Parallel Path Planning with Multiple Evasion Strategies," *Proceedings of the IEEE International Conference on Robotics and Automation* (2002) pp. 1232–1237. Washington, DC, USA.
9. H. Tanner, S. Loizou and K. Kyriakopoulos, "Nonholonomic navigation and control of cooperating mobile manipulators," *IEEE Trans. Robot. Autom.* **19**(1), (2003) pp. 53–64.
10. B. Hussien, Robot Path Planning and Obstacle Avoidance by Means of Potential Function Method. *Ph.D. Dissertation* (Columbia, MO: University of Missouri-Columbia, 1989).
11. E. Rimon and D. E. Koditschek, "Exact robot navigation using artificial potential functions," *IEEE Trans. Robot. Autom.* **8**(5), 501–518 (1992).
12. K. J. Kyriakopoulos, P. Kakambouras and N. J. Krikelis, "Navigation of Nonholonomic Vehicle in Complex Environments with Potential Field and Tracking," *Proceedings of the IEEE International Conference on Robotics and Automation* (1996) pp. 3389–3394. Minneapolis, MN, USA.
13. R. A. Conn and M. Kam, "Robot motion planning on *N*-dimensional star worlds among moving obstacles," *IEEE Trans. Robot. Autom.* **14**(2), 320–325 (1998).
14. J. H. Chuang and N. Ahuja, "An analytically tractable potential field model of free space and its application in obstacle avoidance," *IEEE Trans. Syst. Man Cybern.—Part B: Cybern*. **28**(5), 729–736 (1998).
15. H. Haddad, M. Khatib, S. Lacroix and R. Chatila., "Reactive Navigation in Outdoor Environments using Potential Fields," *Proceedings of the International Conference on Robotics and Automation* (1998) pp. 1232–1237. Leuven, Belgium.
16. D. Fox, W. Burgard and S. Thrun, "The dynamic window approach to collision avoidance," *IEEE Robot. Autom. Mag.* **4**(1), 23–33 (1997).
17. O. Brock and O. Khatib, "High-Speed Navigation Using the Global Dynamic Window Approach," *Proceedings of the IEEE International Conference on Robotics and Automation* (1999) pp. 341–346. Detroit, MI, USA.
18. P. Ogren and N. Leonard, "A convergent dynamic window approach to obstacle avoidance," *IEEE Trans. Robot.* **21**, 188–195 (2005).
19. M. Spenko, K. Iagnemma and S. Dubowsky, "High Speed Hazard Avoidance for Mobile Robots in Rough Terrain," *Proceedings of the SPIE Conference on Unmanned Ground Vehicles* (2004) pp. 439–450, Orland, FL, USA.
20. M. Spenko, Hazard Avoidance for High Speed Rough Terrain Unmanned Ground Vehicles. *Ph.D. Thesis* (Cambridge, MA: Massachusetts Institute of Technology, 2005).
21. A. Stentz, The NAVLAB System for Mobile Robot Navigation, CMU-CS-90-123. *Ph.D. Thesis* (Pittsburgh, PA: School of Computer Science, Carnegie Mellon University, March 1990).
22. J. Dudgeon and R. Gopalakrishnan "Fractal-Based Modeling of 3D Terrain Surfaces." *Proceedings of the IEEE Conference on Bring Together Education, Science, and Technology* (1996) pp. 246–252, Tampa, FL, USA.
23. K. Arakawa and E. Krotkov "Estimating Fractal Dimension from Range Images of Natural Terrain." Technical Report CMU-CS-91-156 (Pittsburgh, PA: School of Computer Science, Carnegie Mellon University, July 1991).
24. K. Iagnemma and S. Dubowsky, *Mobile Robots in Rough Terrain*, STAR Series on Advanced Robotics (Springer, Berlin, 2004).
25. K. D. Iagnemma and S. Dubowsky, "Terrain Estimation for High Speed Rough Terrain Autonomous Vehicle Navigation," *Proceedings of the SPIE Conference on Unmanned Ground Vehicle Technology IV* (2002) pp. 256–266, Orland, FL, USA.
26. P. Bellutta, R. Manduchi, L. Matthies, K. Owens and A. Rankin, "Terrain Perception for DEMO III," *Proceedings of the IEEE Intelligent Vehicles Symposium* (2000) pp. 326–332. Dearborn, MI, USA.
27. D. Golda, K. Iagnemma and S. Dubowsky, "Probabilistic Modeling and Analysis of High-Speed Rough-Terrain Mobile Robots," *Proceedings of the 2004 IEEE International Conference on Robotics and Automation* (2004) pp. 914–919. New Orleans, LA, USA.
28. D. Golda, Modeling and Analysis of High-Speed Mobile Robots Operating on Rough Terrain. *M.S. Thesis* (Cambridge, MA: Massachusetts Institute of Technology, 2003).
29. T. Gillespie, *Fundamentals of Vehicle Dynamics* (Society of Automotive Engineers, Warrendale, PA, 1992).
30. H. Pacejka, "The Tire as a Vehicle Component," *Proceedings of the XXVI FSITA Congress* (1996). Prague, Czech Republic.
31. R. A. Jarvis, "Distance Transform Based Path Planning for Robot Navigation," **In**: *Recent Trends in Mobile Robots*, Y. F. Zheng, ed. (World Scientific, Singapore, (1993) Ch. 1, pp. 3–31.
32. K. Krishna and P. Kalra, "Solving the local minima problem for a mobile robot by classification of spatio-temporal sensory sequences," *J. Robot. Syst.* **17**(10), 549–564 (2000).